



Dike swarms of the west-central Arabian Shield: a key to its tectono-magmatic evolution

Haitham Baggazi¹ · Abdelhamid El-Fakharani^{1,2} · Kamal Ahmed Ali³ · Mohamed K. Elshafei⁴ · Adel Zein Bishta^{5,6}

Received: 28 September 2021 / Accepted: 17 May 2022 / Published online: 30 June 2022
© Geologische Vereinigung e.V. (GV) 2022

Abstract

Dike swarms and structural lineaments were investigated in the Hada Alsham area, west-central Arabian Shield of Saudi Arabia, using remote sensing, field observations, and geochemical analysis techniques. SPOT-7 digital satellite data were employed in the analysis of these structural lineaments and dike swarms. The extracted orientations of the structural lineaments and dike swarms confirm that they are approximately identical, trending mainly in the NNW–WNW, NE–ENE, and E–W directions. Based on field observations and cross-cutting relationships, these dike swarms can be geochronologically arranged (from oldest to youngest) as mafic NNW- to WNW-trending dikes, mafic NE- to ENE-trending dikes, felsic NE-trending dikes, and local mafic E–W dikes. Major and trace elements geochemistry indicates that the studied dike swarms are basalt, basaltic andesite, and rhyolite in composition. Trace and REE diagrams, as well as their immobile elemental ratios of the studied dike swarms suggesting their formation in a typical intraoceanic island arc setting. In addition, the felsic NE dikes may represent extensive fractionation of the mafic magma from which the mafic NE dikes were formed because their incompatible elements signatures are almost similar. All dike swarms were likely emplaced between 620 and 576 Ma, and during the post-collisional extension and relaxation, following the amalgamation of terranes (island arcs) during the collision between the East and West Gondwana.

Keywords Tectonic · Gondwana · Arabian Shield · Geochemical analysis · Dike swarms · Remote sensing

Introduction

East and West Gondwanaland collided during the Pan-African orogeny (950–550 Ma), forming a major Precambrian orogenic belt (Kröner 1984; Stern 1994). Part of this belt is the Arabian–Nubian Shield, which comprises accreted

island arcs and continental fragment terranes from the rifting of Rodinia and the opening of the Mozambique Ocean (> 870 Ma). The amalgamation of these geological terranes occurred along ophiolite suture zones that separate the East and West Gondwana fragments (~ 715–620 Ma) (Stern 1994; Abdelsalam and Stern 1996; Johnson et al. 2011; Abd-Allah et al. 2014; Matsah et al. 2018; Baggazi et al. 2019b; AlKashghari et al. 2020). Generally, post-collisional extension and relaxation (~ 620–540 Ma) reactivated terrane boundaries and are characterized by igneous intrusions of and plutons of linear to curved subvertical dike swarms of various compositions, and different aspects of graben sedimentation (Al-Shanti and Mitchell 1976; Greenwood et al. 1976; Stoeser and Camp 1985; Genna et al. 2002; Collins and Pisarevsky 2005; Johnson et al. 2011; Abd-Allah et al. 2014; Matsah et al. 2018; Baggazi et al. 2019a; El-Fakharani et al. 2019; AlKashghari et al. 2020; El-Fakharani et al. 2020). Igneous intrusions often follow northwest-southeast trending transform faults referred to as the Najd Faults System (NFS). This fault system also accommodated the formation of post-amalgamation basins in the ANS (Genna

✉ Abdelhamid El-Fakharani
abdelsaad@yahoo.com

¹ Structural Geology and Remote Sensing Department, Faculty of Earth Sciences, King Abdulaziz University, P.O. Box 80206, Jeddah 21589, Saudi Arabia
² Geology Department, Faculty of Science, Aswan University, Aswan, Egypt
³ Department of Geosciences, United Arab Emirates University, Al Ain, United Arab Emirates
⁴ Geology Department, Faculty of Science, Suez Canal University, Ismailia, Egypt
⁵ Geoprospection Department, Faculty of Earth Sciences, King Abdulaziz University, Jeddah, Saudi Arabia
⁶ Nuclear Materials Authority, Cairo, Egypt

et al. 2002; Johnson and Woldehaimanot 2003; Johnson et al. 2011; Baggazi et al. 2019b; El-Fakharani et al. 2021) (Fig. 1).

Modern remote sensing techniques offer effective information regarding lithologic discriminations, mineral explorations (Zoheir and Lehmann 2011; Pour et al. 2017; Emam et al. 2018; Matsah et al. 2018; AlKashghari et al.

2020), and lineament extraction which is usually carried out, based on digital satellite image data, either manually (Suzen and Toprak 1998) or automatically (Koike et al. 1998; Casas et al. 2000; Mostafa and Bishta 2005; Bishta 2018) to facilitate structural mapping and mineral explorations. However, automatic alignments extraction could lead to selecting non-structural lineaments such as

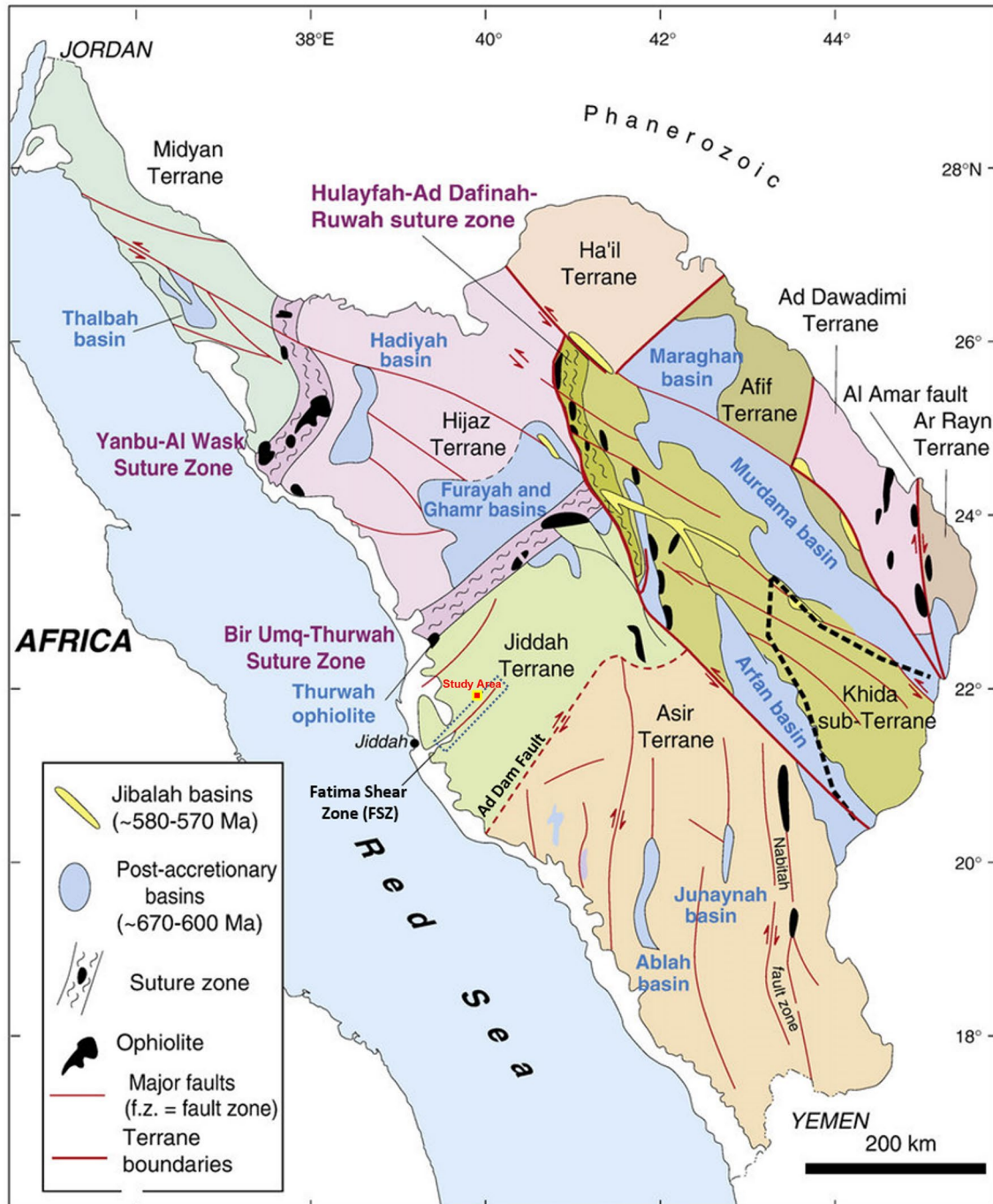


Fig. 1 Tectonic Map of the Arabian Shield (after Nehlig et al. 2002; Johnson and Woldehaimanot 2003). Small rectangle shows the location of the study area

roads, and cliff edges. Therefore, to avoid mixing up lineaments, dikes, and non-structural features, the lineaments and dikes extractions were done manually in this study.

Geochemical analysis is a powerful technique to distinguish dike compositional types and define their tectonic environments, where incompatible element signatures help to determine magma sources and corresponding tectonic settings (Pearce et al. 1984; Rollinson 1993; Hargrove et al. 2006; Abd-Allah et al. 2014; Asran et al. 2017; Pearce and Cann 1971; Pearce 1996).

Volcanic dikes in the western Arabian Shield exhibit different sizes, compositions, and cross-cutting relationships (Matsah et al. 2018). In the study area, dike swarms with different orientations and corresponding field relative ages are presented. Dike swarms of the study area widely vary in thickness and compositions, where they cut the surrounding older metasedimentary, metavolcanic, and granitic rock units. These dike swarms are prominent but do not extend into other younger rocks; their thickness varies from a few centimeters up to several meters across (up not 5 m thick), and extend along strike up to 1 km. These dike swarms also vary in composition and probably formed in different tectonic environments. This study applies remote sensing processes including manual lineaments and dikes extraction from SPOT 7 satellite images,

field observations, and geochemical analysis to identify the geochemical compositions of dike swarms, relationship between structural lineaments and dike swarms, and evaluating the relative age, magma source, and tectonic settings of different types of dike swarms in the study area.

Geological setting and lithology

The study area (Hada Alsham area) is located within the Jiddah terrane and to the north of the NE-oriented Fatima Shear Zone (Fig. 1). The Jiddah terrane contains Cryogenian tectonic ophiolitic rocks, metavolcanic and metasedimentary rocks, volcano-sedimentary rocks, and plutonic intrusions, in addition to Ediacaran sedimentary and subordinate volcanic rocks as well as dikes (Johnson et al. 2011; Johnson and Kattan 2012; Abd-Allah et al. 2014; Matsah et al. 2018; Baggazi et al. 2019a). The area under consideration mainly contains metasedimentary, metavolcanic, and igneous complexes that are intruded by different sets of mafic and felsic dikes that are usually less than 5 m thick (Fig. 2a).

According to Johnson (2006), the Precambrian rocks in the Hada Alsham area are represented by the Samran group, Hishash granite, Kamil suite, and Shayma Nasir group, while Cenozoic rocks are represented by the Haddat

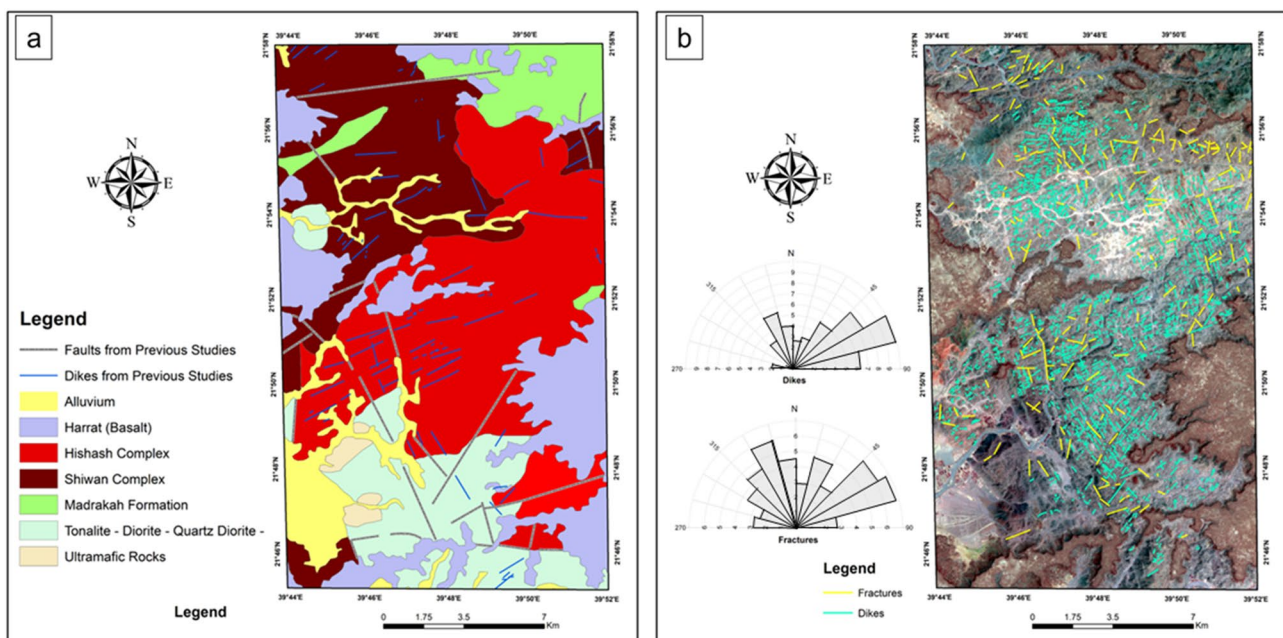
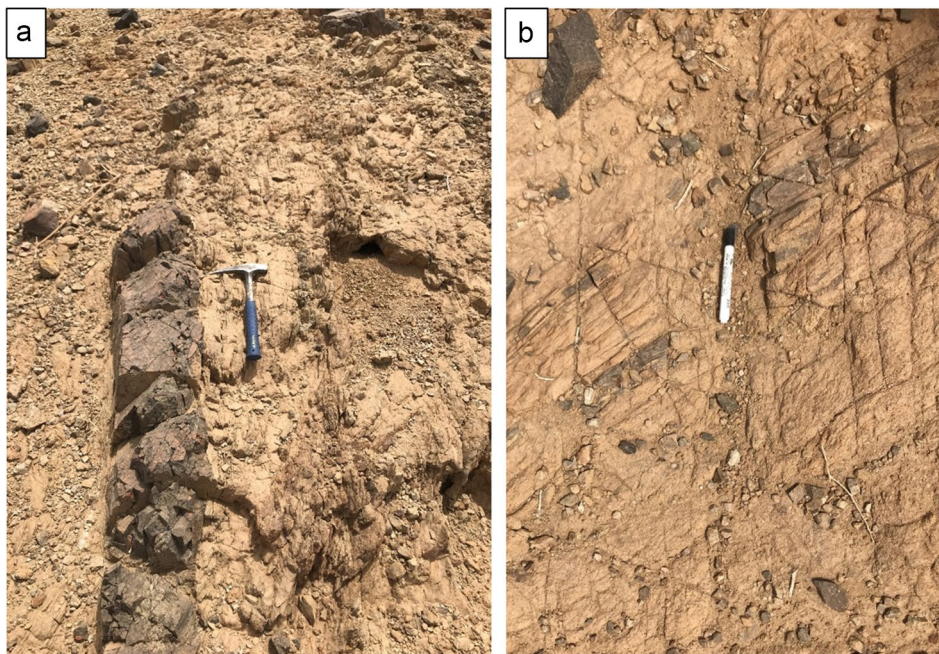


Fig. 2 **a** Geological map of the study area showing major rock units, **b** manually extracted structural lineaments (yellow) and dikes (light blue) from a SPOT-7 satellite image, with associated rose diagrams showing their frequency distribution

Table 1 Summary of main characteristics of all rock units and formations presented in the Hada Alsham area, based on previous studies (Moore and Al-Rehaili 1989)

Stratigraphic units name	Descriptions
Cenozoic units	
Tertiary basalt	Alkalic olivine basalt
Hadat Asham formation	Pebbly sandstone, and siltstone
Precambrian units	
Hishash complex	Massive porphyritic Hornblende-Biotite monzogranite
Shiwan complex	Monzogranite, granodiorite to quartz monzonite, tonalite
Sharqah complex	Interlayered gabbro, norite, diorite, and pyroxenite
Madrakah formation	Basaltic to andesitic lava
Biotite granite	Biotite granite
Diorite tonalite ultramafic	Diorite, tonalite, ultramafic
Jumum formation	Hornblende–quartz–feldspar schist with biotite and garnet schist, and marble

Fig. 3 Field photos showing highly foliated metasedimentary rocks dissected by **a** mafic dikes and **b** different sets of joints with about 15 cm of sinistral displacement



AshSham Formation, Usfan Formation, and basaltic lava (Harrat) flows (Taj 2011). The rocks in the study area (Fig. 2a) encompass Precambrian and Cenozoic units, and more details are provided in Table 1 (Moore and Al-Rehaili 1989; Taj 2011). Slightly foliated Precambrian mafic to felsic dike swarms with different orientations cut the older Precambrian rock units in the study area (Moore and Al-Rehaili 1989). To the south of the study area, similar deformed and mainly NE to ENE and NW to WNW trending mafic and felsic dike swarms intrude the

older Precambrian pre-Fatima basement but not the Fatima Formation, indicating that these dikes are older than the deposition of these Fatima sedimentary rocks (Matsahet al. 2018). The pre-Fatima basement, dike swarms, and the Fatima Formation were affected by NW–SE compression, resulting in the folding and thrusting of the Fatima Formation (Abd-Allah et al. 2014; Matsah et al. 2018; Baggazi et al. 2019a).

The Hada Alsham dikes transect different Precambrian complexes, such as the Shiwan Complex (Rb–Sr age of 769

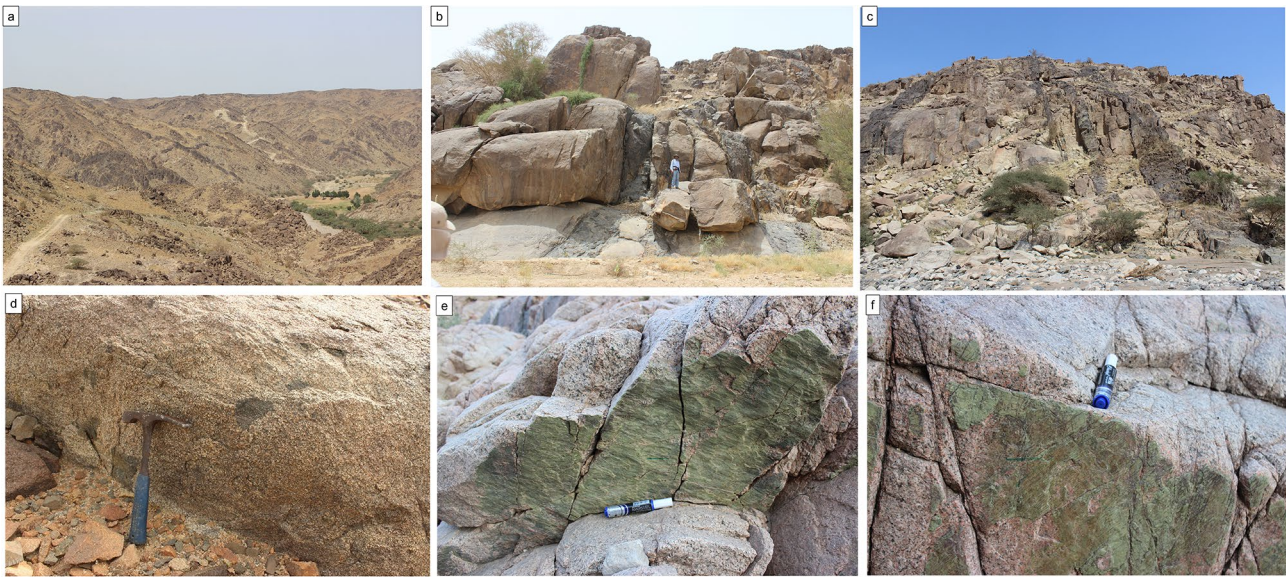


Fig. 4 Fractured granitoid rocks and their hosted dikes, **a** mafic NW- and NNE dikes cutting granitoid host rocks of Shiwan Complex, **b**, **c** sheared mafic NNE-, to NE dikes cutting fractured granitic host rocks

of the Hishash Complex, **d** xenoliths of clustered and/or elongated amphibolite within granite boulder of the Hishash Complex, **e**, **f** NW left lateral faults cutting the Hishash complex granitic rocks

± 39 Ma by Fleck 1981). Moreover, these dikes do not cross-cut the Tertiary Haddat AshSham Formation. To the south of the study area, the dikes in the Wadi Fatima area only transact the rocks of pre-Fatima basement complexes such as the Qattanah Complex (763 ± 159 Ma by Fleck 1981, and Rumayda Complex (773 ± 16 Ma by Duyverman et al. 1982). Additionally, the Rb–Sr ages for the lava and igneous bodies within the Fatima Formation are 576 ± 28 Ma and 592 ± 23 Ma, respectively (Moore and Al-Rehaili 1989). Based on the previous age dating and field relationships, the mafic and felsic dike swarms in the Hada Alsham area and Wadi Fatima area (to the south) were emplaced between < 763 Ma and > 576 Ma.

Methodology and results

Different methods and techniques are adopted in this study, including (1) lineament and dike orientation analysis based on satellite images, (2) field observations, measurements, and relationships, and (3) geochemical analysis techniques. These techniques and analytical methods are described below together with their corresponding results.

Lineament and dike extraction

Digital SPOT-7 data were processed in ArcMap to manually extract the structural lineaments likely fractures, faults, and dikes. The extracted structural lineaments in the study area exhibit trends that cluster in the NNE–ENE direction, NNW–NW direction, and E–W direction. Additionally, a statistical analysis of extracted dike swarms reveals that these dikes attain almost similar NE–ENE, NNW–NW, and E–W trends (Fig. 2b). Since the thickness of the dikes are relatively small (< 5 m thick), and the structural lineaments and dike trends are consistent with each other, and many of the dikes have thickness (up to 5 m thick), both are likely formed during the same tectonic events following the regional stress patterns at the time of emplacement rather than any pre-existing structures.

Field observations

Different rock types and cross-cutting relationships were observed in the field. These rocks are classified into three main groups: (1) host or country rocks, including ultramafic

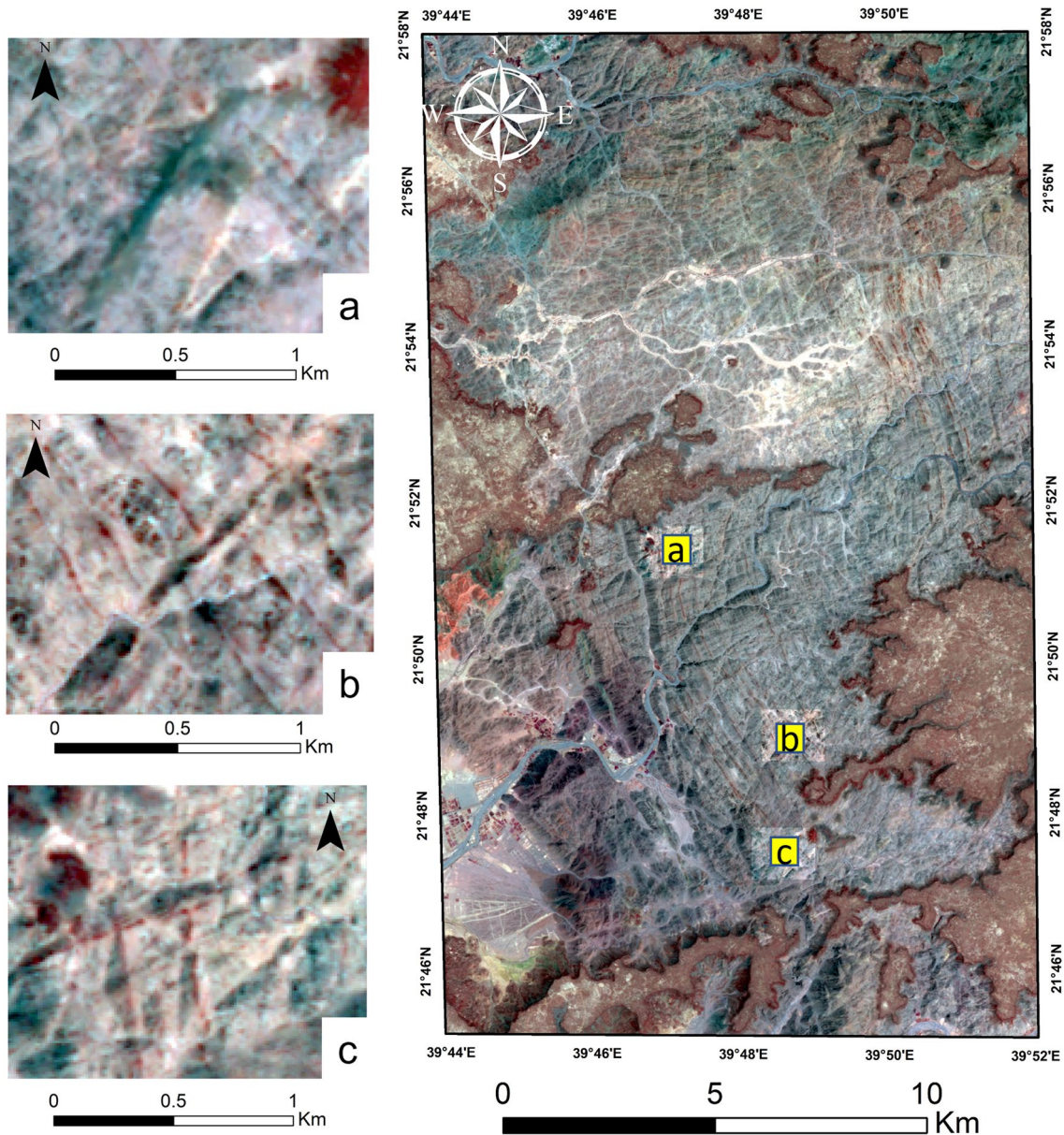


Fig. 5 Spot-7 satellite image of the rocks of Hada Alsham area, **a**, **b** mafic NNE dikes cutting the mafic NW dikes, **c** mafic ENE dikes cutting the mafic N–S to NNW dikes

rocks, metasedimentary rocks, and granitic rocks; (2) hosted dike swarms of different compositions and orientations, including mafic dikes mostly trending NNW- to NW (mafic NNW dikes), mafic dikes mostly trending NE- to ENE (mafic NE dikes), felsic dikes mostly trending NE, and mafic dikes mostly trending E–W directions; and (3) tertiary rocks, including the Haddat AshSham Formation and basalt flows (Harrat). The rocks in the study area are described below in chronological order.

The ultramafic rocks are the oldest rock unite in the study area, which are very scarce and found only as elongated spots in the lower SW corner of the mapped area (Fig. 2a). The ultramafic units are highly deformed, metamorphosed and contain dark-green serpentinized pyroxenite and are crosscut by Precambrian intrusions related to the Hishash Complex (Moore and Al-Rehaili 1989).

Metasedimentary rocks are also not widely distributed in the study area; they mostly described from the most



Fig. 6 Dikes field relationship, **a**, **b**, and **d** mafic NE dike cuts a mafic NNW dike hosted by granitic rocks of the Hishash Complex, **c** a felsic NE dike cuts a mafic NNW dike hosted by granitic rocks of the Shiwan Complex

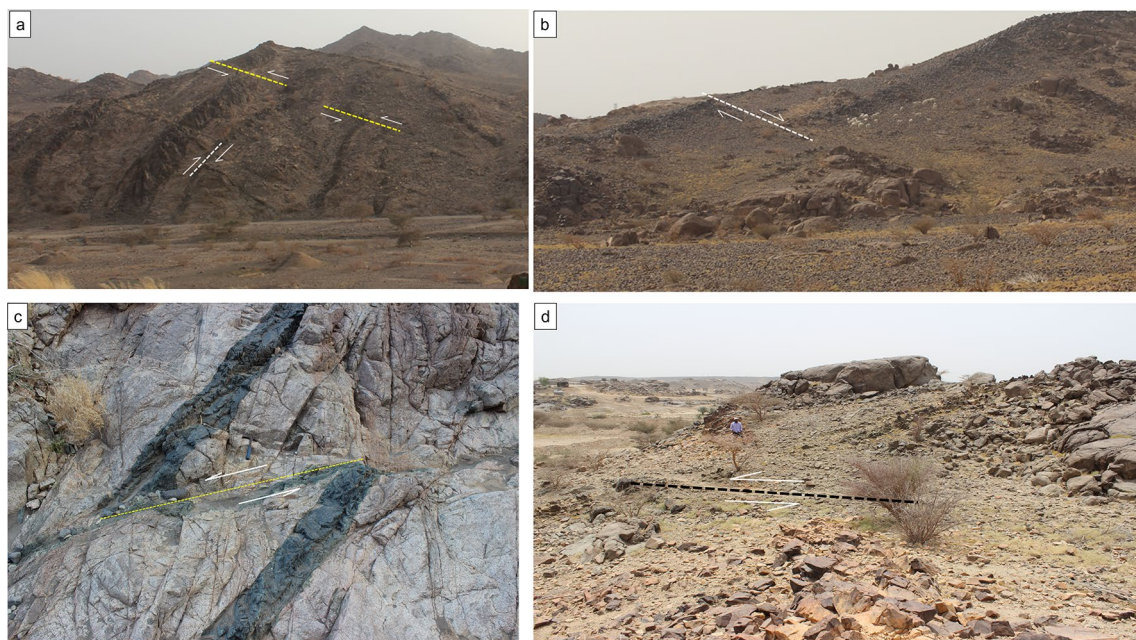


Fig. 7 Different dike directions cut by faults, **a** right lateral fault (white dashed line) cuts thin mafic NNW dikes, and left lateral faults (yellow dashed line) cut mafic NE dikes, **b** right lateral fault cuts mafic NW dike, **c** mafic E–W dike along left lateral fault that cuts mafic NE dike, **d** left lateral fault that cuts felsic NE dike

Table 2 Major and trace elements of dike swarms samples collected from the Hada Alsham area

Sample	NNW dikes			NE basalt dikes										EW dikes										NE rhyolite dikes				
	H10C	H6B	W30B	H1E	W39C	KH3A	KH2B	W40B	W41B	H6A	H7B	W33C	H10A	W25B	W38B	H8A	W33B1	W33B2	W35B	W37B								
SiO ₂	56.4	50.8	55.8	48.7	53.4	51.2	50.6	54.0	52.7	54.6	50.5	55.4	57.9	52.2	76.2	76.3	73.6	72.9	76.0	73.2								
Al ₂ O ₃	17.6	17.6	16.4	16.8	17.4	16.7	17.8	18.7	15.8	16.0	16.2	17.5	17.3	19.0	12.2	12.5	14.0	14.0	12.6	13.1								
Fe ₂ O ₃	7.7	9.3	7.4	10.8	8.9	8.8	10.2	8.3	11.5	9.5	11.3	9.5	7.7	9.6	2.1	1.3	2.2	2.7	1.3	2.7								
CaO	7.4	8.8	6.4	9.3	6.4	8.2	9.0	4.1	4.9	5.7	7.9	5.9	2.1	7.9	0.6	0.6	1.0	1.0	0.7	1.5								
MgO	2.6	5.1	4.4	6.3	3.9	6.4	5.0	4.2	4.1	3.9	4.5	3.6	3.6	3.7	0.2	0.1	0.2	0.2	0.1	0.8								
Na ₂ O	3.3	3.2	4.3	2.4	4.3	3.2	2.5	5.7	5.4	4.7	3.5	3.9	7.4	5.0	4.5	3.9	4.5	4.8	3.9	4.3								
K ₂ O	1.75	0.86	1.34	1.66	1.61	0.82	1.23	1.72	1.25	1.04	0.78	1.75	1.29	0.88	2.97	4.07	3.79	3.28	3.95	3.14								
MnO	0.16	0.16	0.12	0.17	0.14	0.14	0.17	0.17	0.18	0.17	0.18	0.18	0.13	0.16	0.03	0.03	0.05	0.05	0.02	0.06								
TiO ₂	0.85	0.82	0.86	0.86	1.19	1.17	0.8	0.92	1.42	1.14	1.15	0.79	0.77	0.94	0.13	0.05	0.1	0.13	0.04	0.22								
P ₂ O ₅	0.21	0.16	0.2	0.1	0.3	0.23	0.13	0.21	0.4	0.32	0.23	0.16	0.22	0.21	0.02	0.02	0.03	0.03	0.01	0.03								
LOI	1.8	3.0	2.5	2.6	2.3	2.9	2.3	1.7	2.3	2.7	3.5	1.1	1.5	0.3	0.9	0.9	0.5	0.8	1.2	0.9								
Sum	99.82	99.78	99.79	99.75	99.79	99.76	99.79	99.78	99.78	99.78	99.76	99.82	99.85	99.8	99.95	99.96	99.93	99.93	99.96	99.9								
Ga	17.2	16.8	17.6	15.5	17.4	15.6	17.8	19.4	16.6	17.8	18.1	17.6	16.9	18.9	13.3	12.4	13.3	14.4	13.5	16.1								
Hf	3.6	1.6	2.8	1.2	2.9	4.1	1.8	2.2	3.8	3.1	2.2	2.1	2.6	1.9	4.9	3	4.7	4.9	3.1	5.4								
Nb	2.4	1.1	1.7	0.8	2.6	2.2	0.9	1.7	2.5	2.1	1.2	1.3	1.9	1.4	4.3	2.9	3.2	3.1	2.8	4.8								
Rb	47.3	16.2	26.3	49.9	42.7	23.4	27.3	51.6	21.2	15.9	12.7	50.9	26	13.9	50.5	89.4	66.9	60.1	87.1	48.3								
Sn	<1	<1	<1	<1	<1	<1	<1	<1	<1	<1	<1	<1	2	<1	<1	2	<1	<1	2	<1								
Sr	458	440	501	370	481	464	384	537	232	432	441	380	180	373	74	83	153	185	60	123								
Ta	0.1	<0.1	<0.1	<0.1	0.2	<0.1	<0.1	0.1	0.2	0.2	<0.1	<0.1	<0.1	0.1	0.3	0.3	0.2	0.3	0.3	0.3								
Th	1.9	0.3	1	0.5	1	0.8	0.4	0.7	0.9	0.9	0.5	0.7	0.9	0.5	3.4	5.7	4.4	3.8	5.3	3.8								
U	0.9	0.2	0.4	0.3	0.3	0.4	0.2	0.4	0.5	0.3	0.2	0.4	0.4	0.3	1.6	2.1	2.2	1.8	2.4	1.5								
V	177	241	183	326	219	180	250	215	301	257	307	220	154	260	<8	<8	<8	<8	<8	21								
Zr	131.2	55	93.7	35.3	107.7	175.7	58.2	81.9	138.1	112.6	74.6	71.1	93.9	61	154.3	71.5	149.2	165.3	73.4	168.4								
Y	22.5	18	13.9	14.4	16	25.2	21.9	16.4	31.3	24.2	21	22.2	18.9	19.2	34.7	27	27.3	25.5	28	32.7								
La	11.7	5.6	9.5	5.4	12.7	10.3	5.2	9.6	14.3	11	8	8.6	10.1	10.1	20.1	18.6	20.7	17.2	19.5	23.2								
Ce	25.1	12.3	20.5	9.7	26.8	23	11.6	19.3	32.5	25.2	17.5	16.9	21.3	16.8	38.6	37.5	37.4	36.9	38.4	49.9								
Pr	3.63	1.88	2.91	1.44	3.88	3.39	1.8	2.84	4.71	3.77	2.67	2.47	3.05	2.51	5.13	4.69	4.89	4.52	4.84	6.24								
Nd	16.5	9.1	13.3	7.2	17.7	15.6	8.7	13	22.3	17.4	13.5	11.8	14.1	12.2	21.4	18.3	19	17.9	19.3	24								
Sm	3.72	2.62	3.08	1.95	3.74	3.97	2.57	3.04	5.4	4.17	3.36	3.06	3.24	3.07	4.5	3.89	4.13	3.79	4.18	5.13								
Eu	1.03	0.88	0.93	0.77	1.33	1.33	0.89	1.04	1.56	1.31	1.1	1.03	0.9	1.06	0.72	0.38	0.62	0.74	0.38	0.71								
Gd	4.09	2.94	2.99	2.34	3.88	4.4	3.14	3.2	5.78	4.58	3.77	3.58	3.43	3.35	4.79	4.07	3.88	3.72	4.15	4.94								
Tb	0.63	0.49	0.44	0.4	0.55	0.71	0.57	0.51	0.94	0.7	0.61	0.59	0.54	0.56	0.84	0.67	0.68	0.63	0.69	0.85								
Dy	3.81	3.21	2.46	2.49	3.27	4.37	3.61	3.04	5.44	4.11	3.77	3.75	3.29	3.33	5.32	4.26	4.47	3.83	4.31	5.61								
Ho	0.85	0.67	0.5	0.55	0.63	0.95	0.82	0.65	1.14	0.89	0.79	0.78	0.69	0.7	1.2	0.92	0.89	0.87	0.92	1.13								
Er	2.39	2.06	1.63	1.54	1.74	2.77	2.44	1.74	3.29	2.53	2.27	2.46	1.95	2.18	3.79	2.87	2.98	2.87	2.84	3.43								
Tm	0.33	0.28	0.22	0.22	0.22	0.38	0.36	0.24	0.46	0.35	0.33	0.36	0.3	0.3	0.57	0.43	0.46	0.45	0.44	0.54								

Table 2 (continued)

Sample	NNW dikes					NE basalt dikes					EW dikes					NE rhyolite dikes				
	H10C	H6B	W30B	H1E	W39C	KH3A	KH2B	W40B	W41B	H6A	H7B	W33C	H10A	W25B	W38B	H8A	W33B1	W33B2	W35B	W37B
Yb	2.27	1.83	1.37	1.46	1.49	2.48	2.27	1.66	3.14	2.36	2.17	2.37	2	2	3.77	2.8	3.1	3.06	3.02	3.67
Lu	0.35	0.3	0.21	0.22	0.22	0.37	0.37	0.28	0.46	0.38	0.34	0.37	0.32	0.29	0.57	0.46	0.5	0.48	0.45	0.58
Ni	<20	29	44	<20	27	85	<20	<20	<20	<20	<20	<20	<20	<20	<20	<20	<20	<20	<20	<20
Cr	27.4	68.4	116.3	109.5	68.4	157.3	20.5	27.4	13.7	<13.7	34.2	<13.7	<13.7	34.2	<13.7	<13.7	<13.7	<13.7	<13.7	34.2
Mg#	40.3	52.1	54.0	53.7	46.0	59.1	49.3	50.4	41.3	45.1	44.1	42.6	48.6	43.6	14.5	10.6	12.3	15.0	9.4	37.1
Co	20.1	30.1	25.1	39	26.1	35.6	30.4	24	31.7	25.8	32.4	24.3	19	25.5	1.1	0.6	0.8	1.4	0.6	5
La/Nb	4.9	5.1	5.6	6.8	4.9	4.7	5.8	5.6	5.7	5.2	6.7	6.6	5.3	7.2	4.7	6.4	6.5	5.5	7.0	4.8
(La/Yb) _N	3.5	2.1	4.7	2.5	5.8	2.8	1.6	3.9	3.1	3.2	2.5	2.5	3.4	3.4	3.6	4.5	4.5	3.8	4.4	4.3

Major (wt.%), trace and REE (ppm) elements were determined by ICP-AES (major elements) and ICP-MS

northeastern corner and, to a lesser extent, in the north-western part of the study area (Fig. 2a). The metasedimentary rocks belong to the Madrasah Formation (Moore and Al-Rehaili 1989), which is encountered in the NW and NE corners of the mapped area (Fig. 2a) and is elongated in a NE–SW direction. They are highly foliated, sheared, and altered, outcropping as dark brown to yellowish-brown exposures. The metasedimentary rocks are cut by Precambrian mafic dikes of different orientations but mainly parallel to the foliation direction, and both the host rocks and dikes are cut by different fracture sets (Fig. 3). The rocks of the Madrasah Formation forms a part of the Samran Group and are unconformably overlain by the Fatima Group. The Madrasah group rocks consist of andesitic to basaltic lavas, andesitic volcanoclastic rocks, and pyroclastic rocks combined with meta-sandstone and marble. Regional greenschist facies metamorphism affected the Madrasah Formation that is intruded by a tonalite pluton with an Rb–Sr age of 759 ± 39 Ma (Fleck 1981).

Tonalite-diorite-quartz diorite plutons are the third oldest rock units in the study area and occur as isolated spots along the southern border of the mapped area (Fig. 2a). These rock units are intruded by the Shiwan Complex, which is described later. The plutons are rather melanocratic and contain approximately 35% hornblende and biotite (Moore and Al-Rehaili 1989). Tonalite deformation could have been related to the NE-SW Fatima shear zone event (Moore and Al-Rehaili 1989), which underwent dextral transpression prior to the formation of the Fatima basin (Abd-Allah et al. 2014; Baggazi et al. 2019a).

Other igneous intrusions (diorite, granodiorite, and monzogranite) in the study area are very common in the north-western part of the study area (Fig. 2a). These igneous rocks belong to the Shiwan Complex, which is part of a Kamil Suite and consists of hornblende tonalite, hornblende-biotite tonalite, quartz diorite, diorite, granodiorite, and monzonite (Johnson 2006). The Shiwan Complex is transected mainly by mafic NW and NE dikes (Fig. 4a). The Shiwan complex is overlain by Fatima Group rocks, which contain lavas with K–Ar ages of 576 ± 28 Ma (Brown et al. 1978) and 592 ± 23 Ma (Duyverman et al. 1982). In the southern and northeastern parts of the study area, other igneous rocks belong to the Hishash Complex (Fig. 2a), which intrude ultramafic rocks, metasedimentary rocks (the Madrasah Formation), tonalite, diorite and quartz diorite, as well as the Shiwan Complex (Moore and Al-Rehaili 1989). The pinkish to gray Hishash Complex is cut by various dikes and fractures of different orientations (Fig. 4b–d), and also transected by NW trending left-lateral faults (Fig. 4e, f). In hand specimens, the rocks of Hishash Complex mainly comprise quartz, orthoclase, plagioclase, with minor muscovite, biotite, and opaque minerals.

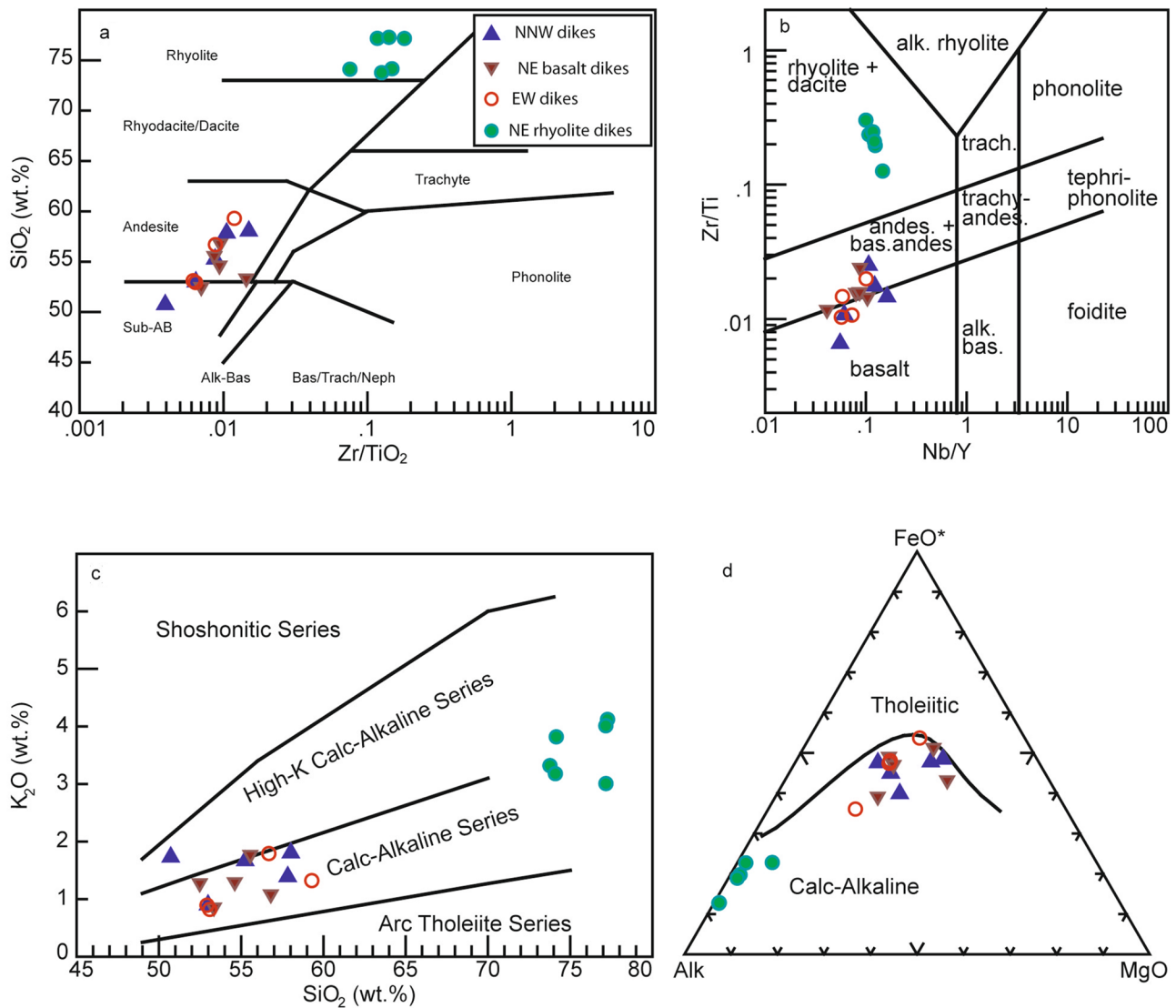


Fig. 8 Major elements and compatible trace elements for dike swarms from Hada Alsham area, Saudi Arabia. **a** Zr/TiO_2 versus SiO_2 diagram (Winchester and Floyd 1977) showing that the studied dikes are of two major types, mafic and rhyolitic; **b** Nb/Yb versus Zr/Ti diagram (Winchester and Floyd 1977) showing that the NNW, NE–ENE,

and NE mafic dikes are basaltic and basalt andesite, and andesite; **c** SiO_2 versus K_2O relationship (Le Maitre 1989); and **d** AFM diagram ($A = Na_2O + K_2O$; $F = FeO^*$; $M = MgO$). Calc-alkaline-tholeiitic boundary (solid curve) as proposed by Irvine and Baragar (1971), showing that the studied samples are calc-alkaline

Dike swarms

Generally, dikes are formed when magma fills fractures, which are normally the result of tensional, shear, or compressional regimes (e.g., Ragland et al. 1983; Ernst et al. 1995; Hamilton et al. 2001; Philpotts and Ague 2022). The tectonic setting during the formation of dikes plays an important role in the type of magma that rise and fill

fractures. In the study area, dike swarms with different orientations, thicknesses (up to 5 m), and compositions cut the metasedimentary, metavolcanic, and granitic rock units. These dike swarms are prominent but do not extend into other younger rocks, such as the Haddat AshSham, Alshoumasi, and Fatima Formations. Relative cross-cutting mafic dike relationship can be determined from satellite images.

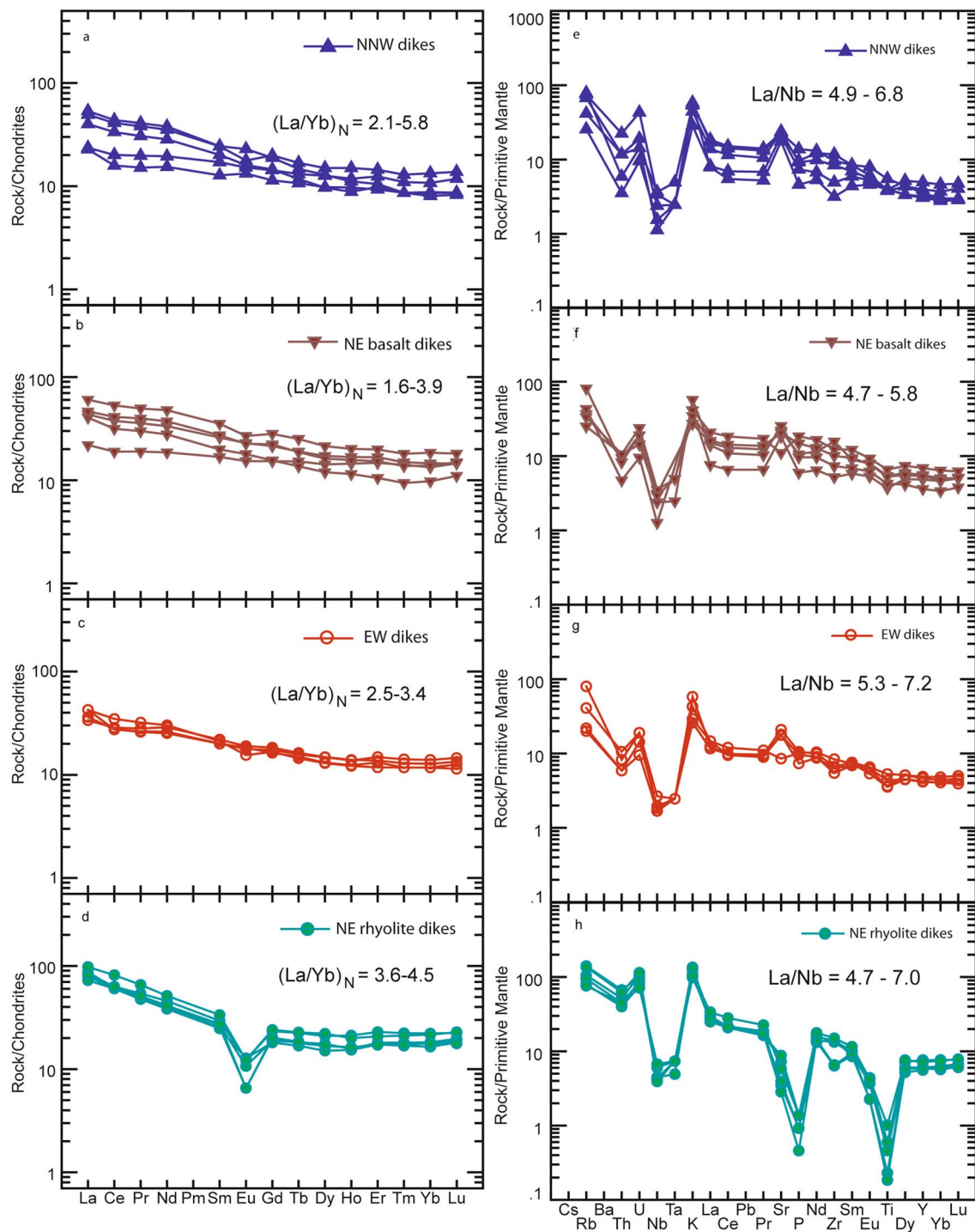


Fig. 9 Chondrite-normalized rare earth element (REE) patterns and primitive mantle-normalized trace element spider diagrams for the dike swarms. (All elements are normalized to the values of chondrite and primitive mantle reported by Sun and McDonough (1989))

The mafic NNE- and ENE-trending dikes are younger than the mafic NNW- to NW-trending dikes (Fig. 5a–c).

Field and crosscutting relationships (Fig. 6a–d) in addition to satellite image analysis (Fig. 5a–c) revealed that these dike swarms could be chronologically arranged as mafic N-S

to NNW trending dikes, mafic NW trending dikes, mafic NE to ENE trending dikes, and rhyolitic NE dikes.

Mafic NW–SE trending dikes The orientations of mafic NW trending dikes generally trend between N10° and 60° W, with certain dikes even trending in an N–S direction (Fig. 5).

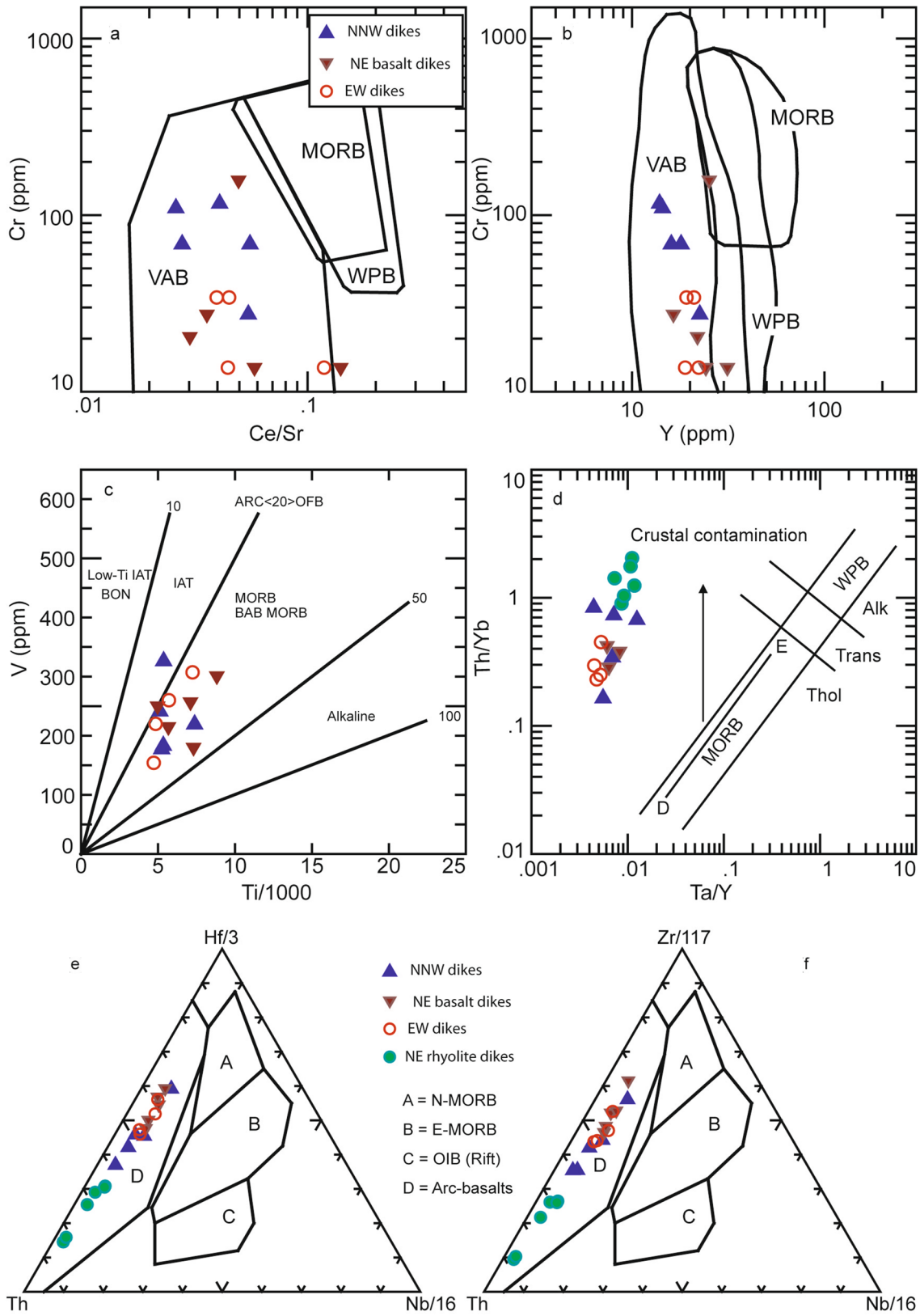


Fig. 10 Trace element discrimination diagrams for mafic and intermediate lavas from different tectonic settings showing data for dike swarms samples: **a** (F) Cr–Ce/Sr (Pearce 1996); **b** Cr–Y (Pearce et al. 1981); **c** V–Ti/1000 (Shervais 1982); **d** Th/Yb–Ta/Yb (Pearce et al. 1981); **e** Th–Hf/3–Nb/116 (Wood, 1980); and **f** Th–Zr/117–Nb/16 (Wood 1980). *WPB* within-plate basalt, *MORB* mid-ocean ridge basalt, *E-MORB* enriched mid-ocean ridge basalt, *VAB* volcanic-arc basalt, *BAB* back-arc basalt, *IAT* island-arc tholeiitic, *OIB* ocean island basalt, *Thol* tholeiitic, *Alk* alkali, *Tran* transitional, *C-A* basalt-alkali basalt

Based on field crosscutting relations with other dikes, these represent the oldest dikes in the study area (Fig. 6). These dikes vary in length from a few meters to more than 1 km and from a thickness of a few centimeters up to 5 m in width. These dikes are highly fractured, fine- to medium-grained, and range in composition from basalt and basaltic andesites to andesites with a light gray to grayish-green color. These mafic NW trending dikes are highly fractured and jointed by at least three sets of vertical joints that systematically trend NNE-SSW, NE-SW and WNW-ESE. At certain locations, the mafic NW-trending dikes are displaced by right-laterally movement along NE-SW trending faults (Fig. 7a, b).

Mafic NE–SW trending dikes These mafic NE trending dikes generally trend between N30° and 70° E and are younger than the mafic NW-trending dikes (Fig. 6a–c). These dikes are only slightly deformed and mainly basaltic in composition. They attain thicknesses ranging from 0.5 m to a few tens of meters (Fig. 7). At certain locations, mafic NE-trending dikes are generally transected by sinistrally displaced along E–W trending faults (Fig. 7a, c) that have been utilized by thin mafic E–W trending dikes (Fig. 7c), indicating that these thin mafic E–W trending dikes are the youngest.

Felsic NE–SW trending dikes Rhyolitic NE trending dikes are scarce, light yellowish red to dark red in color and exhibit fine-grained aphyric to porphyritic textures. The dikes range in thickness from a few centimeters to a few meters and extend up to a few hundreds of meters. In addition, these dikes are highly fractured and displaced by E–W trending sinistral faults (Fig. 7d). Cross-cutting relationship with the mafic NW dikes indicates that these rhyolitic NE dikes are younger (Fig. 6d).

Tertiary rock units

Tertiary rocks are common and represented by the Haddat AshSham Formation and basaltic flows (Harrat) (Fig. 2a). The Haddat AshSham Formation rests unconformably on Precambrian units and consists of conglomerates, sandstone, thin beds of shale, and shaly siltstones (Moore and Al-Rehaili 1989). These clastic beds are very conspicuous where they reveal variations in both color and thickness. Additionally, they are typically faulted and slightly to moderately dipping to the east. The basaltic flows occur as cap rocks horizontally

cover any older rock units and comprise thick plateaus ranging in thickness from a few meters up to a few tens of meters. In hand specimens, these basaltic rocks exhibit a gray to grayish black color and a fine-grained texture with an occasional vesicles (Moore and Al-Rehaili 1989).

Geochemical analysis

Analytical techniques

Twenty-three samples were analyzed for major and trace elements using inductively coupled plasma-atomic emission spectrometry (ICP-AES) and inductively coupled plasma-mass spectrometry (ICP-MS), respectively, at the ACME Analytical Laboratories Ltd., Canada. The prepared powders of selected sample (0.100 g) are added to lithium metaborate/lithium tetraborate flux, mixed well and fused in a furnace at 1025 °C. The resulting melt is then cooled and dissolved in an acid mixture containing nitric, hydrochloric, and hydrofluoric acids. This solution is then analyzed by ICP-AES and ICP-MS for major, trace and REE, and the results are corrected for spectral inter-element interferences. Analytical precision, as calculated from replicate analyses, is better than 0.5% for major elements and varies from 2 to 5% for trace element. Duplicate crushed and pulverized (pulp duplicate) fractions are also analyzed to define samples homogeneity and analytical precision. A blank and certified standard reference materials (CRMs) STD SO-15 are used to monitor the accuracy of the analysis. Major, trace, and REE contents of the analyzed dike samples are listed in Table 2.

Bulk major, trace, and rare-earth elements compositions

The process of hydrothermal fluid and rock interactions is complex and could involve changes in the mineral composition, texture, and chemical composition of the host rocks (Pirajno and Smithies 1992). Hydrothermal alteration of rocks can remove and introduce large amounts of more mobile elements such as Na₂O, K₂O, Rb, Sr, MgO and CaO, while rare earth elements (REEs) and high-field-strength elements (HFSEs) remain more immobile (Polat and Hofmann 2003). Therefore, the least altered samples were selected for geochemical analysis. Since alteration typically hydrates and or carbonates a rock, alteration minerals, such as calcite, actinolite, and chlorite, will break down at 1050 °C and the resulting loss of ignition (LOI) can assist in the investigation of the elemental distribution extent due to the presence of any excess H₂O and/or CO₂ (Ali et al. 2009). The LOI in the studied volcanic samples ranges from 0.3 to 3.5 wt.% (mean = 1.7%), indicating that most of the samples are only slightly altered. The samples obtained from the study area reveal large variations in Cr₂O₃ (< 13.7–157.3 ppm) and

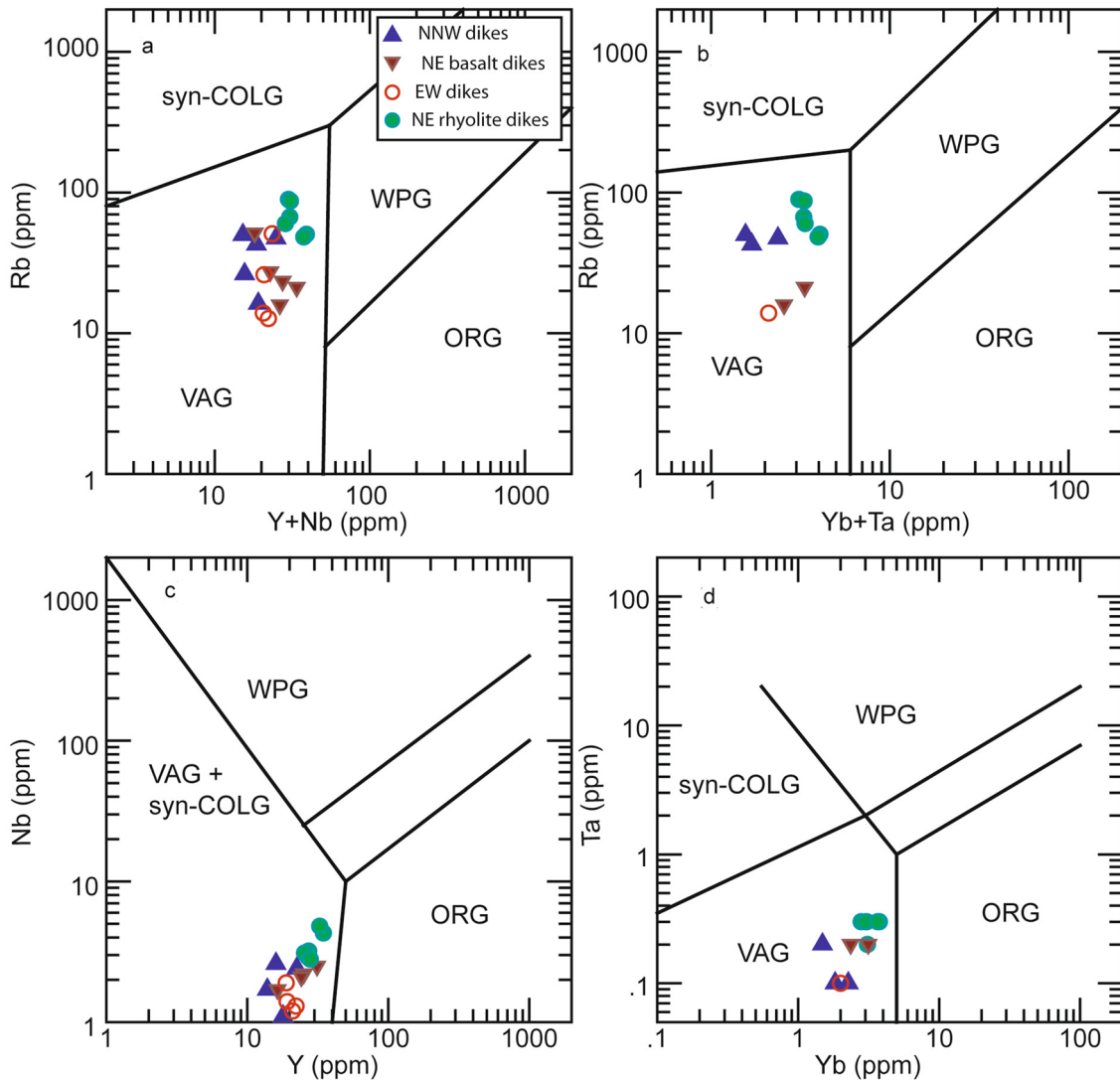


Fig. 11 Trace elements tectonic discrimination diagrams. **a** Y+Nb vs. Rb; **b** Yb+Nb vs. Rb, **c** Y vs. Nb, and **d** Yb vs. Ta diagrams (after Pearce et al. 1984), showing the studied samples have been formed in a volcanic-arc/syn-collisional tectonic setting (VAG+syn-

COLG). VAG volcanic arc granite, *syn-COLG* syn-collision granite, *ORG* ocean ridge granite, *WPG* within plate granitum *post-COLG* post-collisional granite

NiO (<20–85 ppm) contents, as well as Mg# (= $100 \times \text{MgO} / (\text{MgO} + \text{FeO})$) (9.4–59.1) (Table 2).

A classification diagram by Winchester and Floyd (1977) (Fig. 8a) indicates that the samples mainly include basalts, basaltic andesites, and rhyolites. The same rock types are indicated by the Nb/Y vs. Zr/Ti diagram revised by Pearce (1996), originally developed by Winchester and Floyd (1977). Thus, the mafic NW, NE, and E–W dike samples plot in the basalt, basaltic andesite and andesite fields, respectively, while the felsic NE dike samples plot in the rhyolite field (Fig. 8b).

The studied dikes indicate broad ranges of SiO₂ (48.7–76.3 wt.%; Fig. 8c), TiO₂ (0.04–1.42 wt.%), Al₂O₃

(12.22–18.95 wt.%), K₂O (0.78–4.07 wt.%), and MgO (0.07–6.40 wt.%). The Le Maitre et al. (1989) diagram of K₂O against SiO₂ shows that the studied mafic NW-, NE- and E–W-trending dikes all belong to the same low-to medium-K suites, whereas the felsic NE-trending dikes extend into the high calc-alkaline series (Fig. 8c). In the AFM diagram (c.f., Irvine and Baragar, 1971; Fig. 8d), all dike swarms plot in the calc-alkaline field.

Trace element data further reveal the following geochemical characteristics: (1) La/Nb is generally > 1.1 (4.7 to 7.0), suggesting a typical tectonic setting of an intraoceanic island arc (Straub 1995); (2) spider diagrams (Fig. 9e–h) show large-ion lithophile elements (LILE)

enrichment (Rb, K, Sr), and depletion of Ta, Nb, and Ti, which also typical for subduction zones; and (3) the REE patterns (Fig. 9a–d) are slightly fractionated, i.e., mafic NW dikes: $[(La/Yb)_N = 2.1–5.8]$, mafic NE dikes: $[(La/Yb)_N = 1.6–3.9]$, mafic E–W dikes: $[(La/Yb)_N = 2.5–3.4]$, and felsic NE dikes: $[(La/Yb)_N = 3.6–4.5]$. The felsic NE dike samples have negative Eu anomalies (Fig. 9d). The heavy rare earth element (HREE) flat patterns indicate that elemental partitioning during melting or fractionation was not controlled by garnet.

Discussion and conclusions

Tectonic setting implication

Important trace and minor elements (e.g., Zr, Yb, Cr, Ti, Y, Th and V) and corresponding ratios can help infer the tectonic setting of the studied samples. The tectonic setting of the dike samples was inferred based on an analysis of different discrimination diagrams (Fig. 10). The following provides a discussion of the geochemical results based on each of these discrimination diagrams:

Visualization of our data in a Cr-(Ce/Sr) Cartesian diagram (Fig. 10a; Pearce 1982) demonstrates that all samples plot in the volcanic arc basalt (VAB) field. According to Ali et al. (2009), this diagram may be used for less alteration rocks. Relatively low Ce/Sr and low Cr contents are typical for VAB. In the Cr–Y tectonic discrimination diagram (Fig. 10b; Pearce et al. 1981), all samples plot in the VAB field. The Ti–V discrimination diagram (Fig. 10c; Shervais 1982) is highly recommended to distinguish different tectonic settings, such as mid-ocean ridge basalt (MORB), within-plate basalt (WPB) and tholeiitic arc basalt (TAB). This diagram indicates that most samples plot in the field of mid-ocean ridge basalt (MORB) and back-arc basalt (BAB), except for one sample that plots in the island arc tholeiite (IAT) field. Because Ti and V exhibit different behaviors in basaltic melts, this diagram is very sensitive and easily distinguishes tectonic settings as a consequence of partitioning changes with the oxygen fugacity. Consequently, MORB and WPB are less sensitive to oxidation than arc magmas (Rollinson, 1993). Th/Yb–Ta/Yb is one of the most effective discrimination diagrams (Fig. 10d; Pearce et al. 1981) because, in the absence of garnet in the residuum (Fig. 9), the Th/Yb ratios do not change much during melting and fractionation and are typically higher in subduction-related magmas. This occurs because This added to the mantle melt via flux melting during the subduction process, whereas Ta is not. Therefore, any change in Th versus Ta is clearly indicated in this discrimination diagram. All studied samples plot above the mantle array, suggesting

that the corresponding arc magmas were generated in a convergent margin setting and/or became mixed with continental crust materials. The last ternary Th–Hf/3-Nb/16 and Th–Zr/117-Nb/16 diagrams (Fig. 10e, f; Wood 1980) reveal that all dike magmas were formed in an arc tectonic setting.

The tectonic setting of the felsic dikes (rhyolites) can be determined with the same discrimination diagrams as those considered for plutonic granite rocks (Stern et al. 1991). All felsic NE trending dikes plot in the volcanic arc/syn-collisional fields (VAG + syn-COLG) in the Y + Nb vs. Rb, Yb + Ta vs. Rb, Y vs. Nb, and Yb vs. Ta diagrams (Fig. 11a–d) (Pearce et al. 1984). The mafic and intermediate dikes—added for comparison—also plot in the same volcanic arc/syn-collisional fields. In addition, the petrogenesis of the felsic NE-trending dikes may represent extensive fractionation of the mafic magma, which intruded prior to these as mafic NE dikes, because their incompatible elements signatures are so similar (Fig. 9).

In conclusion, the cross-cutting field relationships and geochemical analysis results of the dike swarms confirm that the relative age order (from oldest to youngest) of the dikes is mafic NW dikes, mafic NE dikes, felsic NE dikes, and then mafic E–W dikes. Based on their similar incompatible element signatures, felsic NE dikes likely represent extreme differentiates from mafic NE dikes. Various geochemical discrimination diagrams and multi-elements diagrams consistently confirm that all dike swarms of the studied area in the west-central Arabian Shield formed within a volcanic arc/syn-collisional setting. Based on field relationships and geochemical discrimination diagrams, the dike swarms were likely emplaced during post-collisional extension and relaxation (~620–575 Ma) following upon the collision between the East and West Gondwana fragments (~715–620 Ma). Moreover, the dikes are younger than the Shiwan Complex (~769 Ma) and Madrasah Formation (>759 Ma), and older than the Fatima Group (~576 Ma). Since dikes are tensional features, the dike swarms in the study area were likely emplaced between 620 and 575 Ma.

Acknowledgements This work was supported by the Deanship of Scientific Research (DSR), at King Abdulaziz University, Jeddah, under Grant no. (G:304-145-1440). The authors, therefore, gratefully acknowledge the DSR for technical and financial support. Additionally, the authors are deeply grateful to Dr. Mohamed Matsah (Faculty of Earth Sciences, King Abdulaziz University) for his insightful assistance during the fieldwork. The authors would like to express their gratitude to Prof. Ahmed Hassan for his help and support in editing and reviewing the revised version of the manuscript. The authors also would like to thank Dr M. Klausen and two other anonymous reviewers for their constructive comments on the earlier and revised versions of the manuscript. Professor Wolf-Christian Dullo, the Editor-in-Chief,

and JF Moyen, the Topic Editor, are also highly thanked for their comments and handling of the manuscript.

References

- Abd-Allah A, Ahmed AH, El-Fakharani A, El-Sawy EK, Ali KA (2014) Fatima suture: a new amalgamation zone in the western Arabian Shield, Saudi Arabia. *Precambrian Res* 249:57–78
- Abdelsalam MG, Stern RJ (1996) Sutures and shear zones in the Arabian-Nubian Shield. *J Afr Earth Sc* 23(3):289–310
- Ali KA, Stern RJ, Manton WI, Kimura J, Khamees HA (2009) Geochemistry, Nd isotopes and U-Pb SHRIMP zircon dating of Neoproterozoic volcanic rocks from the Central Eastern Desert of Egypt: New insights into the ~ 750 Ma crust-forming event. *Precambrian Res* 171(1–4):1–22
- AlKashghari WA, Matsah M, Baggazi HM, EL-SawyElfakharaniEl-Shafei EAM (2020) Detection of alteration zones using ASTER imagery and geological field observations: Al Wajh area, North-western Arabian Shield, Saudi Arabia. *Arab J Geosci* 13(16):1–17
- Al-Shanti AM, Mitchell A (1976) Late Precambrian subduction and collision in the Al Amar—Idsas region, Arabian Shield, Kingdom of Saudi Arabia. *Tectonophysics* 30(3–4):T41–T47
- Asran AM, Emam A, El-Fakharani A (2017) Geology, structure, geochemistry and ASTER-based mapping of Neoproterozoic Gebel El-Delhimmi granites, Central Eastern Desert of Egypt. *Lithos* 282(358):372
- Baggazi HM, Abd-Allah AMA, Elfakharani A, Matsah M (2019a) Stress-strain analysis and its tectonic implications for the Fatima suture zone, western Arabian Shield Saudi Arabia. *J Afr Earth Sci* 158:103567
- Baggazi HM, AlKashghari WA, Elfakharani A, Matsah M, El-Shafei MK (2019b) Northern Arabian Shield shear zones: strain analysis comparison. *Arab J Geosci* 12(3):75
- Bishta AZ (2018) Assessment of the reliability of supervised classifications of Landsat-7, ASTER, and SPOT-5 multispectral data in rock unit discriminations of Jabal Daf-Wadi Fatima area, Saudi Arabia. *Arab J Geosci* 11(23):1–21
- Brown GF, Hedge C, Marvin R (1978) Geochronologic data for the Arabian Shield. Sect. 2—Tabulation of Rb-Sr and K-Ar ages given by rocks of the Arabian Shield, Rep.US geol.Surv.Saudi Arabian Project, vol. 240, pp 10–22
- Casas AM, Cortes AL, Maestro A, Soriano MA, Riaguas A, Bernal J (2000) LINDENS: a program for lineament length and density analysis. *Comput Geosci* 26(9–10):1011–1022
- Collins AS, Pisarevsky SA (2005) Amalgamating eastern Gondwana: the evolution of the Circum-Indian Orogens. *Earth Sci Rev* 71(3–4):229–270
- Duyverman HJ, Harris NBW, Hawkesworth CJ (1982) Crustal accretion in the Pan African: Nd and Sr isotope evidence from the Arabian Shield. *Earth Planet Sci Lett* 59(2):315–326
- El-Fakharani A, Abd-Allah A, El-Sawy EK, Hamimi Z, Shujoon A (2019) Emplacement levels and pre-existing structures control mechanisms and host rock interactions of three granitic plutons, western Arabian Shield. *Int J Earth Sci* 108(4):1233–1251
- El-Fakharani A, AlKashghari WA, Baggazi HM, El-Shafei M, Matsah M (2020) Microstructural analyses of the Najd Fault System in Midyan Terrane NW Arabian Shield, Saudi Arabia. *Int J Earth Sci* 109(1):301–316
- El-Fakharani A, Radwan A, Hagag W, Abdel-Rahman E, Younis MH (2021) Structural and petrological re-assessed for the Najd-related shear zones along the Egyptian Eastern Desert. *Arab J Geosci* 14(12):1–22
- Emam A, Hamimi Z, El-Fakharani A, Abdel-Rahman E, Barreiro JG, Abo-Soliman MY (2018) Utilization of ASTER and OLI data for lithological mapping of Nugrus-Hafafit area, South Eastern Desert of Egypt. *Arab J Geosci* 11(23):1–22
- Ernst RE, Head WJ, Parfitt E, Grosfils E, Wilson L (1995) Giant radiating dike swarms on Earth and Venus. *Earth-Sci Rev* 39:1–58
- Fleck RJ (1981) Age of diorite-granodiorite gneisses of the Jiddah-Makkah region, Kingdom of Saudi Arabia, Ministry of Petroleum and Mineral Resources, Deputy Ministry for Mineral
- Genna A, Nehlig P, Le Goff E, Guerrot C, Shanti M (2002) Proterozoic tectonism of the Arabian Shield. *Precambrian Res* 117(1–2):21–40
- Greenwood WR, Hadley DG, Anderson RE, Fleck RJ, Schmidt DL (1976) A Discussion on global tectonics in Proterozoic times-Late Proterozoic cratonization in southwest Saudi Arabia. *Philos Trans R Soc Lond Ser Math Phys Sci* 280(1298):517–527
- Hamilton MA, Goutier J, Mathews W (2001) U-Pb baddeleyite age for the Paleoproterozoic Lac Esprit dyke swarm, James Bay region, Quebec: Radiogenic age and isotopic studies. Report 14. Geological Survey of Canada, Current Research 2001-F5, p 10
- Hargrove US, Stern RJ, Kimura JI, Manton WI, Johnson R (2006) How juvenile Arabian-Nubian Shield? Evidence from Nd isotopes and pre-Neoproterozoic inherited zircon in the Bi'rUmq suture zone, Saudi Arabia. *Earth Planet Sci Lett* 252(308):326
- Irvine TN, Baragar W (1971) A guide to the chemical classification of the common volcanic rocks. *Can J Earth Sci* 8(5):523–548
- Johnson PR (2006) Explanatory notes to the map of Proterozoic geology of western Saudi Arabia, Saudi Geological Survey Technical Report SGS-TR-2006–4, vol. 62
- Johnson PR, Kattan FK (2012) The geology of the Arabian Shield, A review of the geology of Precambrian rocks, Kingdom of Saudi Arabia.SGS. Special Publication, Riyadh
- Johnson PR, Woldehaimanot B (2003) Development of the Arabian-Nubian Shield: perspectives on accretion and deformation in the northern East African Orogen and the assembly of Gondwana. *Geol Soc Lond Spec Publ* 206(1):289–325
- Johnson PR, Andresen A, Collins AS, Fowler AR, Fritz H, Ghebreab W, Kusky T, Stern RJ (2011) Late Cryogenian-Ediacaran history of the Arabian-Nubian Shield: a review of depositional, plutonic, structural, and tectonic events in the closing stages of the northern East African Orogen. *J Afr Earth Sci* 61(3):167–232
- Koike K, Nagano S, Kawaba K (1998) Construction and analysis of interpreted fracture planes through combination of satellite-image derived lineaments and digital elevation model data. *Comput Geosci* 24(6):573–583
- Kröner A (1984) Evolution, growth and stabilization of the Precambrian lithosphere. *Phys Chem Earth* 15:69–106
- Le Maitre RW, Bateman P, Dudek A, Keller J, Lameyre J, Le Bas MJ, Zanettin, B (1989) A classification of igneous rocks and glossary of terms. In Recommendations of the IUGS subcommission on the Systematics of Igneous rocks. London: Blackwell Scientific Publications. vol. 193
- Matsah MI, Baggazi HM, El Fakharani A, El-Shafei M (2018) Deformed dike swarms as an implication of transpression deformation in Western Arabian shield Wadi Fatima, Saudi Arabia. *Arab J Geosci* 11(22):1–10
- Moore TA, Al-Rehaili MH (1989) Geologic map of the Makkah quadrangle, sheet 21D, Kingdom of Saudi Arabia, Saudi Arabian Directorate General of Mineral Resources Geoscience Map GM-107C, scale, vol. 1, no. 250
- Mostafa ME, Bishta AZ (2005) Significance of lineament patterns in rock unit classification and designation: a pilot study on the Gharib-Dara area, northern Eastern Desert, Egypt. *Int J Remote Sens* 26(7):1463–1475
- Nehlig P, Genna A, Asfirane F, Guerrot C, Eberlé JM, Kluyver HM, Lasserre JL, Le Goff E, Nicol N, F. BRGM (2002) A review of the Pan-African evolution of the Arabian Shield. *GeoArabia* 7(1):103–124

- Pearce JA (1996) A user's guide to basalt discrimination diagrams, Trace element geochemistry of volcanic rocks: applications for massive sulphide exploration. *Geol Assoc Can Short Course Notes* 12(79):113
- Pearce J (1982) Trace element characteristics of lavas from destructive plate boundaries. In: Thorpe, RS (Ed.) *Andesites: Orogenic Andesites and Related Rocks*. John Wiley and Sons, pp 525–548
- Pearce JA, Cann JR (1971) Ophiolite origin investigated by discriminant analysis using Ti Zr and Y. *Earth Planet Sci Lett* 12(3):339–349
- Pearce JA, Alabaster T, Shelton AW, Searle MP (1981) The Oman ophiolite as a Cretaceous arc-basin complex: evidence and implications. *Philos Trans R Soc Lond Ser Math Phys Sci* 300(1454):299–317
- Pearce JA, Harris NB, Tindle AG (1984) Trace element discrimination diagrams for the tectonic interpretation of granitic rocks. *J Pe* 25(4):956–983
- Philpotts AR, Ague JJ (2022) *Principles of igneous and metamorphic petrology*. Cambridge University Press
- Pirajno F, Smithies RH (1992) The FeO/(FeO MgO) ratio of tourmaline: a useful indicator of spatial variations in granite-related hydrothermal mineral deposits. *J Geochem Explor* 42(2–3):371–381
- Polat A, Hofmann AW (2003) Alteration and geochemical patterns in the 3.7–3.8 Ga Isua greenstone belt, West Greenland. *Precambrian Res* 126(3–4):197–218
- Pour AB, Hashim M, Park Y (2017) Alteration mineral mapping in inaccessible regions using target detection algorithms to ASTER data. *IOP Publishing. J Phys Conf Ser* 852(1):012022
- Ragland PC, Hatcher RD, Whittington D (1983) Juxtaposed Mesozoic diabase dike sets from the Carolinas. *Geology* 11:394–399
- Rollinson H (1993) A terrane interpretation of the Archaean Limpopo Belt. *Geological Magazine*, 130(6), 755–765. <https://doi.org/10.1017/S001675680002313X>
- Shervais JW (1982) Ti-V plots and the petrogenesis of modern and ophiolitic lavas. *Earth Planet Sci Lett* 59(1):101–118
- Stern RJ (1994) Arc assembly and continental collision in the Neoproterozoic East African Orogen: implications for the consolidation of Gondwanaland. *Annu Rev Earth Planet Sci* 22(1):319–351
- Stern RJ, Kröner A, Rashwan AA (1991) A late Precambrian (~ 710 Ma) high volcanicity rift in the southern Eastern Desert of Egypt. *Geologische Rundschau* 80(1):155–170
- Stoeser DB, Camp VE (1985) Pan-African microplate accretion of the Arabian Shield. *Geol Soc Am Bull* 96(7):817–826
- Straub SM (1995) Contrasting compositions of Mariana Trough fallout tephra and Mariana Island arc volcanics: a fractional crystallization link. *Bull Volcanol* 57(6):403–421
- Sun S, McDonough WF (1989) Chemical and isotopic systematics of oceanic basalts: implications for mantle composition and processes. *Geol Soc Lond Spec Publ* 42(1):313–345
- Suzen ML, Toprak V (1998) Filtering of satellite images in geological lineament analyses: an application to a fault zone in Central Turkey. *Int J Remote Sens* 19(6):1101–1114
- Taj RJ (2011) Stratigraphic setting, facies types and depositional environments of Haddat Ash Sham ironstones, western Arabian Shield, Saudi Arabia. *Asian Trans Basic Appl Sci (ATBAS ISSN: 2221–4293)*, vol. 1, pp. 1–25
- Winchester JA, Floyd PA (1977) Geochemical discrimination of different magma series and their differentiation products using immobile elements. *Chem Geol* 20:325–343
- Wood DA (1980) The application of a ThHfTa diagram to problems of tectonomagmatic classification and to establishing the nature of crustal contamination of basaltic lavas of the British Tertiary Volcanic Province. *Earth Planet Sci Lett* 50(1):11–30
- Zoheir B, Lehmann B (2011) Listvenite–lode association at the Barramiya gold mine Eastern Desert, Egypt. *Ore Geol Rev* 39(1–2):101–115